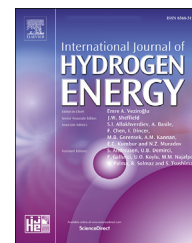


Available online at [www.sciencedirect.com](http://www.sciencedirect.com)

ScienceDirect

journal homepage: [www.elsevier.com/locate/he](http://www.elsevier.com/locate/he)

# Dynamic modeling of preferential CO oxidation in monolithic catalytic reactor using Pt–Fe/ $\gamma$ -Al<sub>2</sub>O<sub>3</sub> catalyst

Gonzalo A. Almeida Pazmiño<sup>a,b</sup>, Dong-Weon Lee<sup>a</sup>, Seunghun Jung<sup>a,\*</sup>

<sup>a</sup> Department of Mechanical Engineering, Chonnam National University, 77 Yongbong-ro, Buk-gu, Gwangju, 61186, Republic of Korea

<sup>b</sup> Escuela Superior Politécnica del Litoral, ESPOL, Facultad de Ingeniería Mecánica y Ciencias de la Producción, Campus Gustavo Galindo Km. 30.5 Vía Perimetral, P.O. Box 09-01-5863, Guayaquil, Ecuador

## HIGHLIGHTS

- Dynamic model of preferential CO oxidation reactor for hydrogen production is developed.
- CO-PROX was simulated under various operating conditions for isothermal and adiabatic reactors.
- Dynamic model was validated with experimental data, which confirmed high fidelity.

## ARTICLE INFO

### Article history:

Received 8 December 2020

Accepted 10 February 2021

Available online 6 March 2021

### Keywords:

Monolithic reactor

Global kinetics

Preferential CO oxidation

Dynamic modeling

## ABSTRACT

This study presents the dynamic modeling of preferential CO oxidation (CO-PROX) over a Pt–Fe/ $\gamma$ -Al<sub>2</sub>O<sub>3</sub> catalyst in a monolithic reactor under both adiabatic and isothermal conditions. The modeling allowed us to investigate the effects of disturbance of the inlet conditions on transient performance. This work includes a mathematical description of the heat- and mass-transfer of species with a quasi-2D approach and a global kinetic mechanism. The model was validated by simulating the steady-state operation of the CO-PROX isothermal reactor and comparison of the predictions with experimental data obtained between 363 and 553 K at atmospheric pressure. The CO-PROX reactor model proved to be robust and accurate in the high-temperature regime (>410 K) and can be used for real-time simulation. The high response sensitivity of the adiabatic reactor predicted a significant improvement in CO conversion at temperatures from 435 K with the addition of a small amount of energy while maintaining a response time of 15 s. The isothermal reactor exhibited a reasonably fast response time when exposed to a realistic gas hourly space velocity scheme based on transient fuel demand in a proton exchange membrane fuel cell system.

© 2021 Hydrogen Energy Publications LLC. Published by Elsevier Ltd. All rights reserved.

\* Corresponding author.

E-mail addresses: [stratus76@hotmail.com](mailto:stratus76@hotmail.com), [stratus760@gmail.com](mailto:stratus760@gmail.com) (S. Jung).

<https://doi.org/10.1016/j.ijhydene.2021.02.084>

0360-3199/© 2021 Hydrogen Energy Publications LLC. Published by Elsevier Ltd. All rights reserved.

## Introduction

Although hydrogen is considered the ultimate clean energy carrier for the future, a significant amount of hydrogen is still produced from fossil fuels through steam reforming (SR), which has an efficiency of 65–75% [1]. However, traces of carbon monoxide (CO) can be found in the SR product (0.5–1%), and this irreversibly degrades Pt-based catalysts in fuel cell electrodes. Thus, the CO concentration in the fuel cell stream must be controlled to be under 10 ppm [2]. For automotive applications such as fuel cell electric vehicles (FCEVs) that require very high-purity hydrogen, two-stage purification involving the water–gas shift (WGS) reaction and highly selective catalytic preferential oxidation (PROX) reaction is preferred [3].

An efficient CO-PROX reaction involves the use of a catalyst with high activity and selectivity for CO oxidation to reduce H<sub>2</sub> consumption. The catalysts mostly used for CO removal in H<sub>2</sub>-rich gases can be sorted into supported noble metal (Pt [4], Ru [5], Au [6]), transition metal (CuO–CeO<sub>2</sub> [2]), complex metal oxides (AuFe–TiO<sub>2</sub> [7]), and intermetallic alloy (Pt–Fe [8]) catalyst. Avgouropoulos et al. [9] presented a comparative analysis of the performance of various catalysts for selective CO oxidation in excess hydrogen. The activity, selectivity, and stability of Pt/Al<sub>2</sub>O<sub>3</sub>, Au/Fe<sub>2</sub>O<sub>3</sub>, and CuO–CeO<sub>2</sub> were evaluated, revealing that Au/Fe<sub>2</sub>O<sub>3</sub> showed relatively high performance at low temperatures (<353–393 K), whereas CuO–CeO<sub>2</sub> seemed to be the most active and selective under high-temperature conditions.

CO-PROX is conducted in a packed-bed catalytic reactor or monolithic catalyst reactor. Because monolithic reactors have compact volumes, low pressure drops, and fast dynamic responses compared with packed-bed catalytic reactors [10], they have received much attention; in particular, cordierite monoliths are popular catalyst supports for CO-PROX applications [11].

Fuel cell systems for automotive applications typically undergo various dynamic conditions such as cold start and feed oscillation. Therefore, the response time and reaction rate and heat generation and distribution of CO-PROX reactors under dynamic conditions are essential for designing and optimizing fuel processing systems for automotive applications. Achieving a fast response time in CO-PROX reactors depends on the low thermal inertia of component materials, small channel size, high inlet temperature, and low gas velocities [12].

Physics-based catalyst modeling is widely used to analyze the kinetics and heat- and mass-transfer phenomena in catalytic reactors and requires the physicochemical properties of the materials and components, as well as detailed elementary chemical kinetics. To date, few publications related to CO-PROX monolithic reactors have been reported, and these have mostly taken a steady-state approach. Ahluwalia et al. [13] obtained experimental data for CO conversion over a Pt-based catalyst on a ceramic monolith to develop an empirical correlation for CO oxidation selectivity and analyze the

multi-stage performance of adiabatic CO-PROX reactors. Jeifetz et al. [14] simulated a one-dimensional heterogeneous model of a monolithic reactor for H<sub>2</sub> stream purification in a proton exchange membrane (PEM) fuel cell, starting with a preliminary isothermal reactor and continuing with different schemes of adiabatic monoliths with inter-stage cooling. Moreno et al. [15] employed the kinetic model for a CuO/CeO<sub>2</sub>/Al<sub>2</sub>O<sub>3</sub> catalytic washcoat and studied the global selectivity toward CO oxidation.

This study investigate the physicochemical phenomena occurring in a CO-PROX monolith reactor theoretically, as well as the transient response to the variation of operating conditions, using a quasi-2D dynamic modeling approach based on an experimental kinetic expression, with the heat and mass-transfer and chemical kinetics on a Pt–Fe/ $\gamma$ -Al<sub>2</sub>O<sub>3</sub> catalyst washcoat.

## Mathematical model

### Model description

The CO-PROX reactor modeled in this study consists of a bundle of monoliths in a substrate where a thin Pt–Fe/ $\gamma$ -Al<sub>2</sub>O<sub>3</sub> catalyst washcoat was uniformly coated onto the walls of the reactor channels, as shown in Fig. 1. Assuming all monoliths are subjected to the same physics, this study considers a single square channel of the CO-PROX reactor. The model is a quasi-2D heterogeneous model incorporating heat and mass transfer in the channel and radial direction. The geometrical parameters, chemical properties, and operating conditions are listed in Tables 1 and 2.

In this dynamic model, the gas mixture is assumed to have a fully developed and incompressible laminar flow, following the ideal-gas law, a negligible pressure drop and axial mass and heat dispersion. Additional assumptions are

- (i) uniform distribution of catalyst loading,
- (ii) uniform average velocity, and
- (iii) negligible volume change of the gas mixture during CO-PROX.

The methodology for the model implementation in MATLAB/Simulink is the same as that reported previously [16]. The thermodynamic and transport properties of gas species were taken from NIST standard reference database 23, v8.0.

### Heat and mass balances

The present dynamic model explores the diffusion of multi-species in the gas mixture, the heat- and mass-transfer process between the gas and solid phase, and the heterogeneous CO selective oxidation on the washcoat surface. The heat and mass balances in the monolith are represented by partial differential equations (PDEs). The CO-PROX reactor model is spatially discretized into sixteen equal-length elements in the axial direction and one radial node to convert the PDEs into

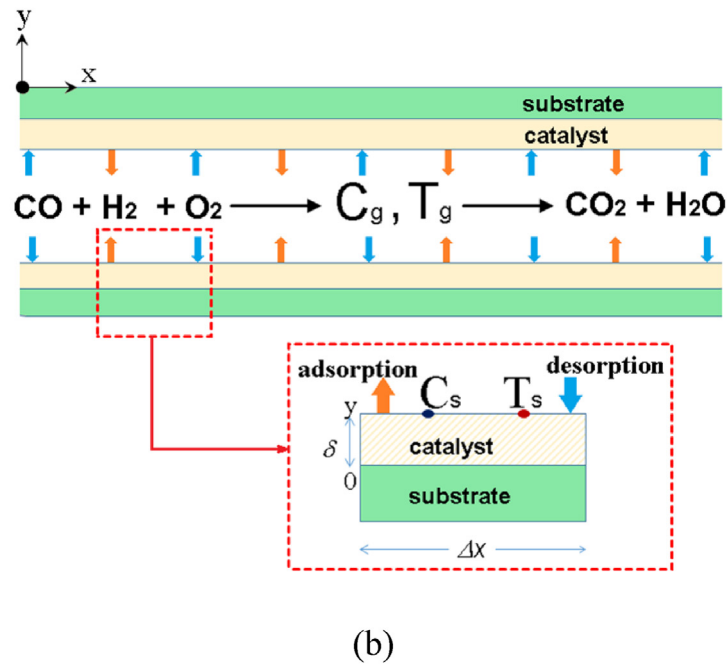
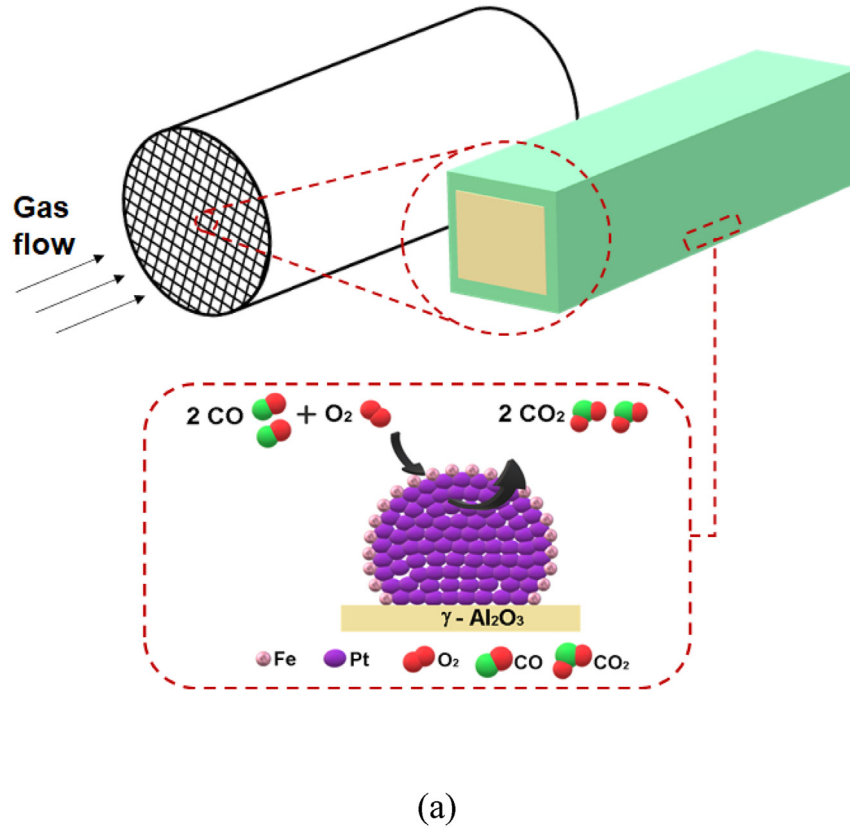


**Fig. 1** – Schematics of the monolithic catalytic reactor: (a) 3D view, and (b) sectional view of a single square channel.

ordinary differential equations (ODEs), as shown in Fig. 1(a). The streamflow and fluid-solid convective mass transfer directions are also regarded in the axial and radial directions.

Fig. 1(b) shows a schematic of the heat and mass transfer in a discretized node of the monolith. The mass balance for

component  $i$  in both the gas phase and washcoat are expressed by Eqs. (1) and (2) [16]:

$$\frac{dC_{i,g}}{dt} = \frac{\bar{u}}{\Delta x} (C_{i,g,in} - C_{i,g}) - \frac{4h_{m,i}}{d_H} (C_{i,g} - C_{i,s}) \quad (1)$$

**Table 1 – Geometric parameters of the monolithic CO-PROX reactor model.**

Description	Symbol	Value	Unit
Channel length	$L_{\text{chn}}$	750.0	mm
Channel width	$W_{\text{chn}}$	95.11E-02	mm
Channel height	$H_{\text{chn}}$	95.11E-02	mm
Washcoat catalyst layer thickness	$\delta$	30.0E-03	mm

**Table 2 – Chemical properties and operating conditions for the CO-PROX model.**

Description	Symbol	Value	Unit
Bulk catalyst density	$\rho_s$	770	kg m <sup>-3</sup>
Catalyst porosity	$\epsilon$	0.4	–
Pressure	$P$	101.3E03	Pa
H <sub>2</sub> inlet concentration	$C_{\text{H}_2,\text{in}}$	64	mol%
CO <sub>2</sub> inlet concentration	$C_{\text{CO}_2,\text{in}}$	2.8	mol%
N <sub>2</sub> inlet concentration	$C_{\text{N}_2,\text{in}}$	balance	mol%

$$(1 - \epsilon) \frac{\rho_g}{M_g} \frac{dC_{i,s}}{dt} = \frac{\rho_g}{M_g} \frac{4h_{\text{mi}}}{D_H} (C_{i,g} - C_{i,s}) + \rho_s \sum_k (a_{i,k} r_k) \quad (2)$$

The heat balance is accordingly expressed as follows:

$$\frac{dT_g}{dt} = \frac{\bar{u}}{\Delta X} (T_{g,\text{in}} - T_g) - \frac{1}{\rho_g c_{p,g}} \frac{4h}{d_H} (T_g - T_s) \quad (3)$$

$$(1 - \epsilon) \rho_s c_{p,s} \frac{dT_s}{dt} = \frac{4h}{D_H} (T_g - T_s) + \rho_s \sum_k (r_k \Delta \bar{H}_k^0) \quad (4)$$

The following are considered boundary and initial conditions:

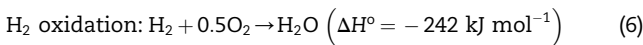
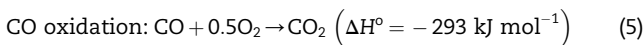
$$\text{Inlet } (z = 0) \quad C_i = C_{i,0}, T_g = T_{g,0}, T_s = T_{s,0}, \frac{dT_s}{dt} = 0$$

$$\text{Initial } (t = 0) \quad C_{i,s} = 0, T_s = T^0.$$

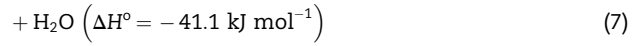
In Eqs. (1) and (3),  $C_{i,g,\text{in}}$  and  $T_{i,g,\text{in}}$  are the species concentration and gas temperature at each computational node, respectively, acquired from the proceeding node's outlet. The  $k$ th reaction rate on the catalyst surface is denoted as  $r_k$  in Eqs. (2) and (4). The set of species involved in the CO-PROX are  $i = \text{CO}, \text{H}_2, \text{O}_2, \text{CO}_2,$  and  $\text{H}_2\text{O}$ . The heat- and mass-transfer coefficients and thermodynamic properties of the gas mixture are summarized in [Appendix A](#).

### Catalytic kinetics

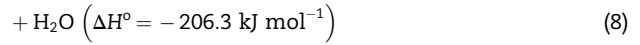
The CO-PROX system involves five reactions, as follows [3]:



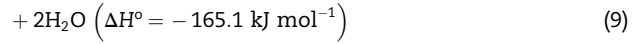
Reverse water – gas shift:  $\text{CO}_2 + \text{H}_2 \leftrightarrow \text{CO}$



CO methanation:  $\text{CO} + 3\text{H}_2 \rightarrow \text{CH}_4$



CO<sub>2</sub> methanation:  $\text{CO}_2 + 4\text{H}_2 \rightarrow \text{CH}_4$



However, the methanation reactions in Eqs. (8) and (9) are considered negligible between 392 and 511 K [18]. Therefore, here, we only consider CO oxidation, H<sub>2</sub> oxidation, and reverse water–gas shift (RWGS) for CO-PROX kinetics.

The two approaches for studying catalytic kinetics are: (i) microkinetics, which involves detailed surface reactions following each reaction step, and (ii) global kinetics, which consists of a simplified explicit rate expression for the overall reaction. Microkinetic modeling presents detailed information regarding the adsorption of reactants from the gas flow on the catalyst surface, surface reactions of the adsorbed species, and desorption of products into the bulk gas mixture; some studies of CO-PROX over Pt-based catalyst can be found in the literature [19,20]. However, microkinetic modeling to simulate CO-PROX with several reaction steps is computationally demanding, especially the investigation of the dynamic physics. Because the present study focuses on the dynamics of CO-PROX, global kinetics was employed.

The following reaction rate expression by Caputo et al. [2] was used for CO oxidation (see Eq. (5)).

$$r_{\text{CO}} = -k_{\text{CO}} P_{\text{CO}}^\alpha P_{\text{O}_2}^\beta \quad (10)$$

where  $P_{\text{CO}}$  and  $P_{\text{O}_2}$  are the CO and O<sub>2</sub> partial pressures,  $\alpha = -0.1$  and  $\beta = 0.5$  are the apparent orders for carbon monoxide and oxygen, and  $k_{\text{CO}}$  is the kinetic constant for CO oxidation.

It is assumed that the kinetics of H<sub>2</sub> oxidation in an H<sub>2</sub>-rich environment follows Eq. (11),

$$r_{\text{H}_2} = -k_{\text{H}_2} P_{\text{O}_2}^\gamma \quad (11)$$

where  $k_{\text{H}_2}$  is the rate coefficient, and  $\gamma = 0.5$  is the apparent reaction order of O<sub>2</sub>.

For the RWGS in Eq. (7), the reaction rate is calculated as in Eq. (12) [24]:

$$r_{\text{rwgs}} = -k_{\text{rwgs}} \left( P_{\text{CO}} P_{\text{H}_2\text{O}} - \frac{P_{\text{CO}_2} P_{\text{H}_2}}{K_{\text{eq}}} \right) \quad (12)$$

$$K_{\text{eq}} = \exp\left(\frac{4577.8}{T} - 4.33\right)$$

where  $K_{\text{eq}}$  and  $k_{\text{rwgs}}$  are the equilibrium constant and rate constant, respectively, for the RWGS.

The following Arrhenius expressions describe the temperature dependence of rate coefficients  $k_{\text{CO}}$ ,  $k_{\text{H}_2}$ , and  $k_{\text{rwgs}}$ :

**Table 3 – Kinetic parameters for CO-PROX [8].**

Description	Symbol	Value	Unit
Pre-exponential factor	$A_{CO}$	3.528E02	$\text{mol atm}^{-0.4} \text{kg}^{-1} \text{s}^{-1}$
Pre-exponential factor	$A_{H_2}$	2.053E01	$\text{mol atm}^{-0.5} \text{kg}^{-1} \text{s}^{-1}$
Pre-exponential factor	$A_{r_{wgs}}$	4.402E03	$\text{mol atm}^{-2.0} \text{kg}^{-1} \text{s}^{-1}$
Activation energy	$E_{a, CO}$	33,092	$\text{J mol}^{-1}$
Activation energy	$E_{a, H_2}$	18,742	$\text{J mol}^{-1}$
Activation energy	$E_{a, r_{wgs}}$	34,104	$\text{J mol}^{-1}$

$$k_{CO} = A_{CO} \exp[-E_{a,CO} / (R_u T_s)] \quad (13)$$

$$k_{H_2} = A_{H_2} \exp[-E_{a,H_2} / (R_u T_s)] \quad (14)$$

$$k_{r_{wgs}} = A_{r_{wgs}} \exp[-E_{a,r_{wgs}} / (R_u T_s)] \quad (15)$$

The kinetics parameters for the commercial “Selectoxo™” catalyst were taken from the report of Choi et al. [8] and are listed in Table 3 for simultaneous CO/H<sub>2</sub> oxidation. Selectoxo™ catalysts are composed of 0.3–0.5% Pt and 0.02% Fe impregnated onto  $\gamma$ -alumina. The catalyst are dried and calcined, and are selective catalyst for the oxidation of CO in H<sub>2</sub>-rich gas.

### Computational procedure

The present model was implemented in MATLAB/Simulink R2019a by applying the multi-domain modeling and simulation technique. Using an Intel® 4.2 GHz i7-7700K CPU with 32 GB of memory (Intel Corporation, Santa Clara, CA, 240 USA), on average, a single simulation took approximately 157.65 s with a relative tolerance of  $10^{-7}$  and max step size of 0.01 via the ODE45 solver.

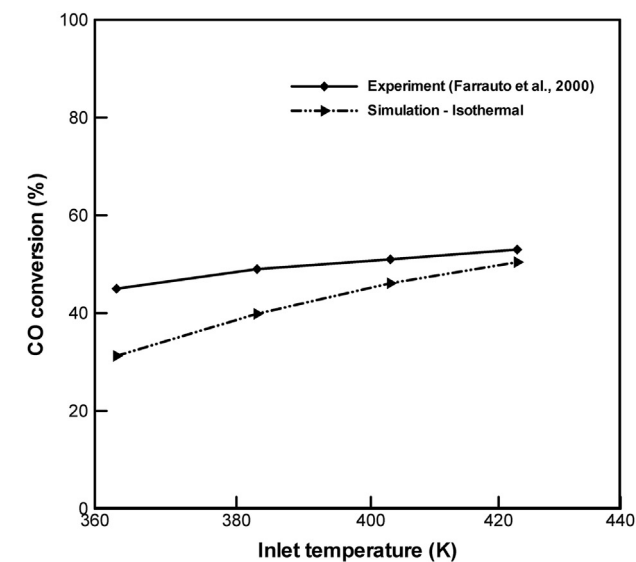
## Result and discussion

In this study, both steady-state and dynamic simulations of the CO-PROX monolithic reactor were carried out. First, steady-state simulations were conducted to investigate the effect of the operating conditions on the reactor performance under both isothermal and adiabatic conditions. Second, the reactor’s dynamic response was predicted and analyzed according to the inlet concentration and reactant temperature changes under the adiabatic condition. Finally, the model’s predicted activity and selectivity were compared with experimental results to confirm its validity.

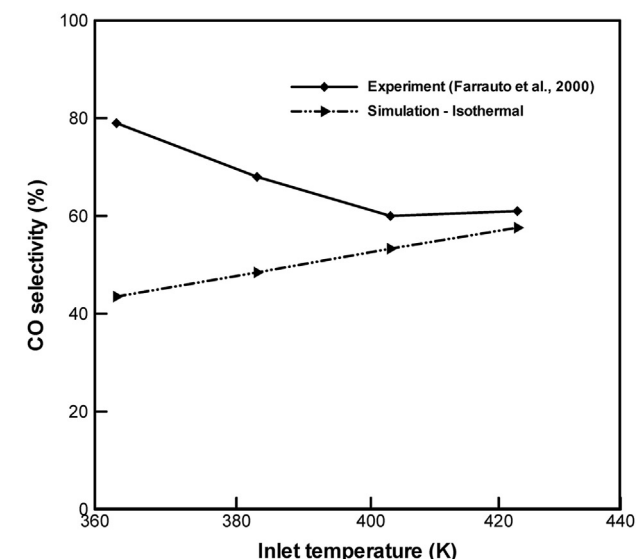
### Steady-state simulation

#### CO conversion and CO selectivity

The performance of the Selectoxo™ catalyst in the CO-PROX reactor has been evaluated in several experimental studies by measuring the catalytic activity and selectivity [8,11,27,28]. The CO conversion ( $X_{CO}$ ) and selectivity ( $S_{CO}$ ) were calculated as shown in Eqs. (16) and (17).



(a)



(b)

**Fig. 2 – (a) Activity and (b) selectivity for CO-PROX depending on the inlet-gas temperature (CO/O<sub>2</sub> = 2; 1000 ppm CO, 20 mol% H<sub>2</sub>; 10 mol% H<sub>2</sub>O; GHSV = 80,000 h<sup>-1</sup>).**

$$X_{CO} = \frac{C_{in,CO} - C_{out,CO}}{C_{in,CO}} \quad (16)$$

$$S_{CO} = \frac{0.5(C_{in,CO} - C_{out,CO})}{C_{in,O_2} - C_{out,O_2}} \quad (17)$$

To remove CO from the reactant gas mixture containing CO

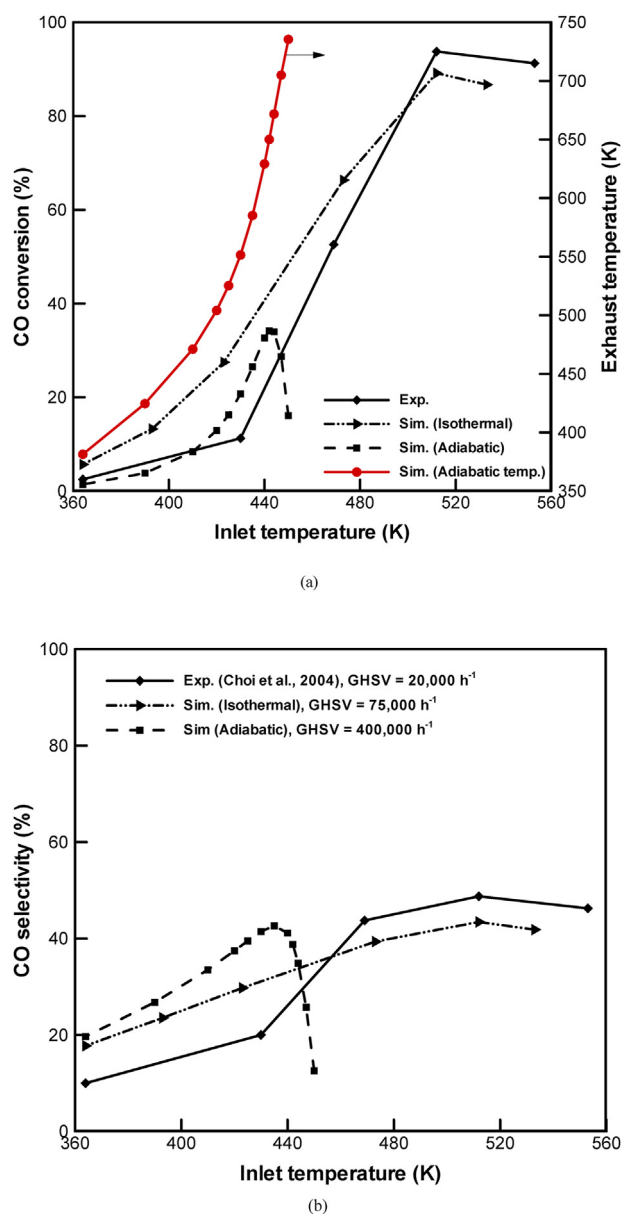


**Fig. 3** – CO (a) conversion and (b) selectivity in the CO-PROX reactor at different inlet-gas temperatures. ( $\text{CO}/\text{O}_2 = 2.8/2.9$ , GHSV of experiment = 20,000 h<sup>-1</sup>, GHSV of simulation (isothermal reactor) = 75,000 h<sup>-1</sup>, GHSV of simulation (adiabatic reactor) = 400,000 h<sup>-1</sup>).

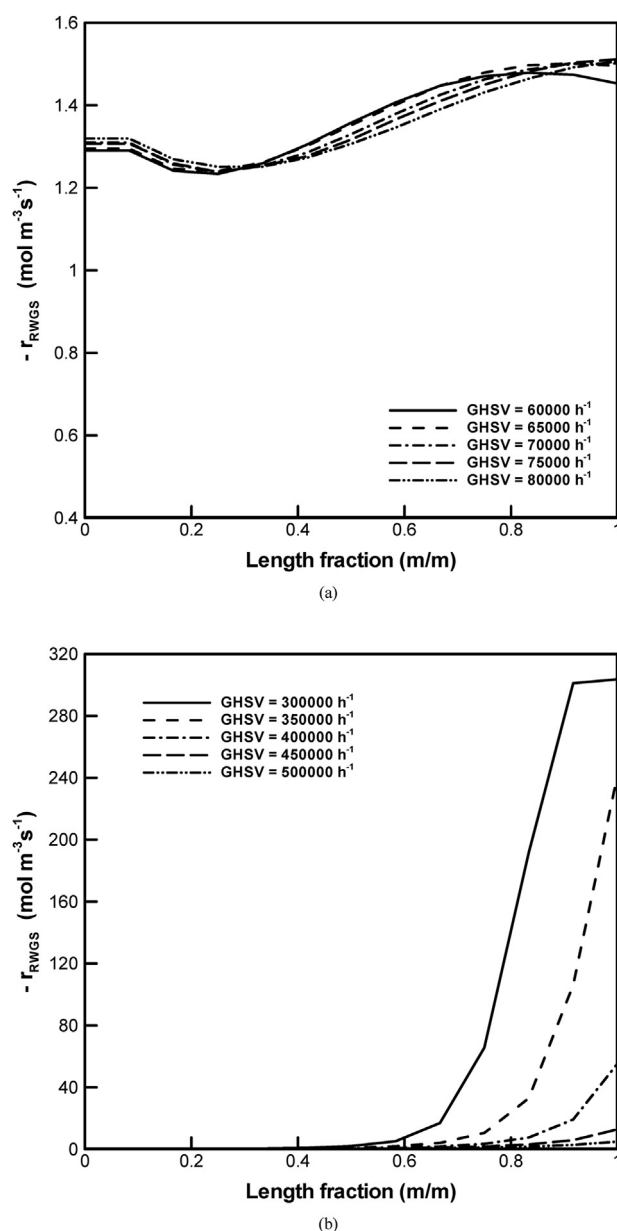


**Fig. 4** – Distribution of the RWGS reaction of the (a) isothermal reactor ( $T_{\text{in},g} = 512$  K) and (b) adiabatic reactor ( $T_{\text{in},g} = 440$  K) at different space velocities ( $\text{CO}/\text{O}_2 = 2.8/2.9$ ).

and H<sub>2</sub>, the supplied O<sub>2</sub> for CO oxidation must combine with CO rather than H<sub>2</sub> in the reactor; this is represented by the “CO selectivity” as defined in Eq. (17).

The simulation results obtained using the present model were compared with the experimental results [27] when the reactor was operated with  $\text{CO}/\text{O}_2 = 2$ ,  $[\text{CO}] = 1000$  ppm,  $[\text{H}_2] = 20$  mol%,  $[\text{H}_2\text{O}] = 10$  mol%, and gas hourly space velocity (GHSV) = 80,000 h<sup>-1</sup> at the reactor inlet under isothermal condition. As presented in Fig. 2(a), the simulated CO conversion, according to the inlet gas temperatures, shows a trend similar to that of the experimental result, although there is a significant deviation in the low-temperature window. The model shows a more significant

deviation from the experimental CO selectivity data, as shown in Fig. 2(b). This difference arises from the presence of H<sub>2</sub>O in the reactant gas mixture. The positive effect of water content on CO-PROX, especially in certain temperature ranges, has been reported in several experimental studies [8,27,29], and this is attributed to a reduction in the activation energy for CO oxidation, as well as the RWGS reaction [30]. However, the kinetic parameters of the present model were acquired with an inlet gas mixture that included 62–72 mol% H<sub>2</sub>, 2.8 mol% CO<sub>2</sub>,  $\text{CO}/\text{O}_2 = 0.5$ –2.0, and no H<sub>2</sub>O. Therefore, this model does not include the influence of H<sub>2</sub>O on CO conversion and selectivity, especially in the low-temperature regime. However, the simulation results agree well with the

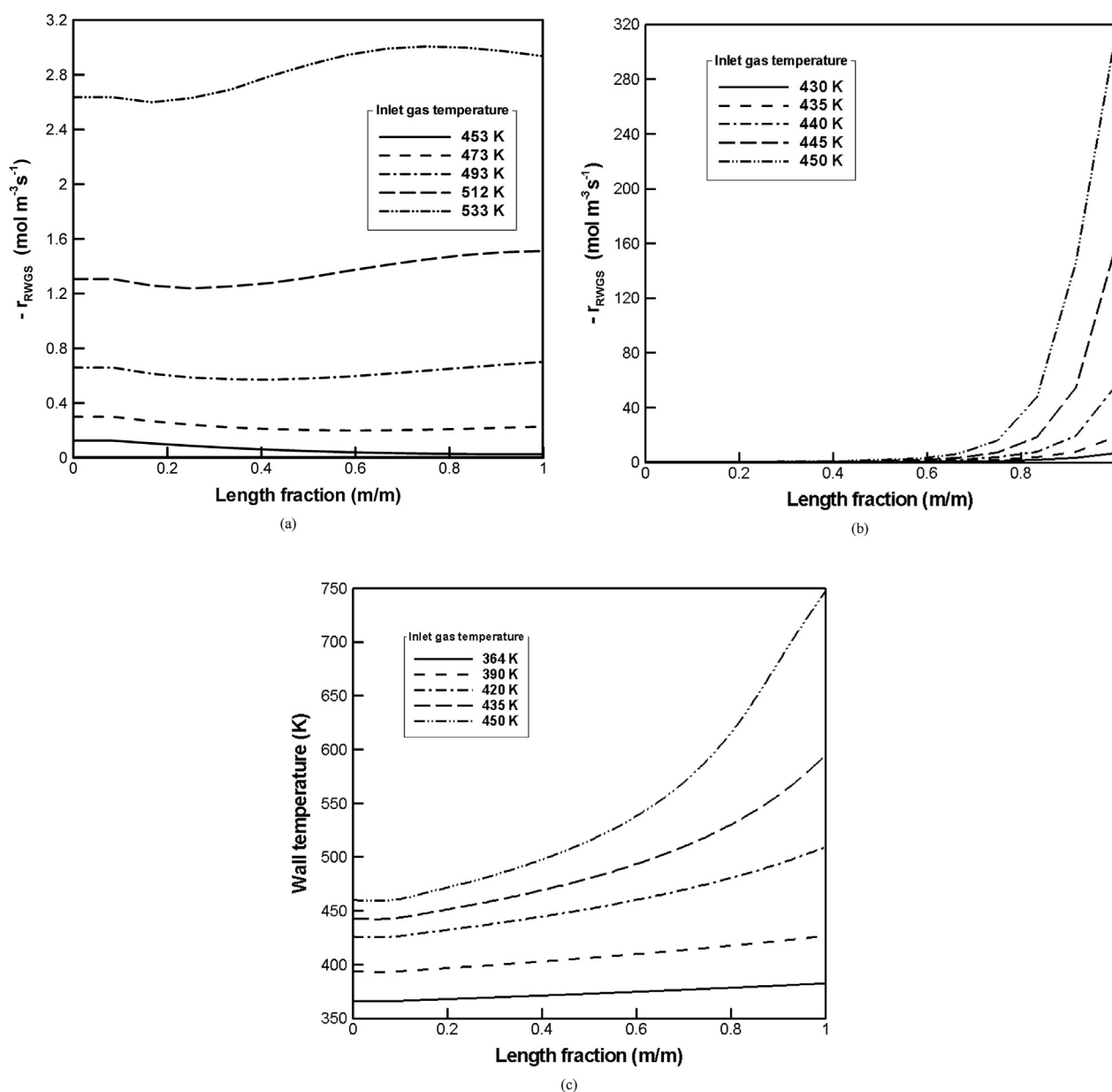


Fig. 5 – (a) Isothermal RWGS ( $\text{GHSV} = 75,000 \text{ h}^{-1}$ ), (b) adiabatic RWGS, and (c) adiabatic wall temperature distribution ( $\text{GHSV} = 400,000 \text{ h}^{-1}$ ) along the CO-PROX reactor at different inlet-gas temperatures ( $\text{CO}/\text{O}_2 = 2.8/2.9$ ).

experimental data in the high-temperature regime ( $>410 \text{ K}$ ), where the actual reactor operates under a negligible  $\text{H}_2\text{O}$  influence.

Packed-bed reactors can achieve catalytic conversion as high as monolithic reactors if they are operated with a lower GHSV than that of monolithic reactors because this results in longer residence times in the reactor [31,32]. Choi et al. [8] measured the catalytic activity and selectivity of Selectoxo and obtained empirical rate expressions for a packed-bed catalytic reactor ( $\text{GHSV} = 20,000 \text{ h}^{-1}$ ) under isothermal conditions. Because the present CO-PROX model is a monolithic reactor, the GHSV of the reactant gas required to achieve the same performance as that of the packed-bed reactor can be determined by comparing the simulation and experimental results, as shown in Fig. 3 for the case at

364–553 K and a  $\text{CO}/\text{O}_2$  feed ratio (C/O) of 2.8/2.9. The isothermal reactor model was simulated with a GHSV of  $75,000 \text{ h}^{-1}$ , whereas the adiabatic reactor model was simulated with a GHSV of  $400,000 \text{ h}^{-1}$ . The catalyst activity increases according to the inlet gas temperature, reaching the highest CO conversion at 512 K under isothermal conditions ( $X_{\text{CO}} = 89\%$ ) and 442 K under the adiabatic condition ( $X_{\text{CO}} = 34\%$ ). However, this conversion begins to fall at higher temperatures in all cases, which can be attributed to the facilitated RWGS reaction producing CO at such high temperatures. In the adiabatic CO-PROX reactor, CO conversion falls steeply because the exhaust gas temperature passes 650 K, as shown in Fig. 3(a).

CO selectivity was observed to improve with an increase in temperature, as shown in Fig. 3(b), reaching the maximum at

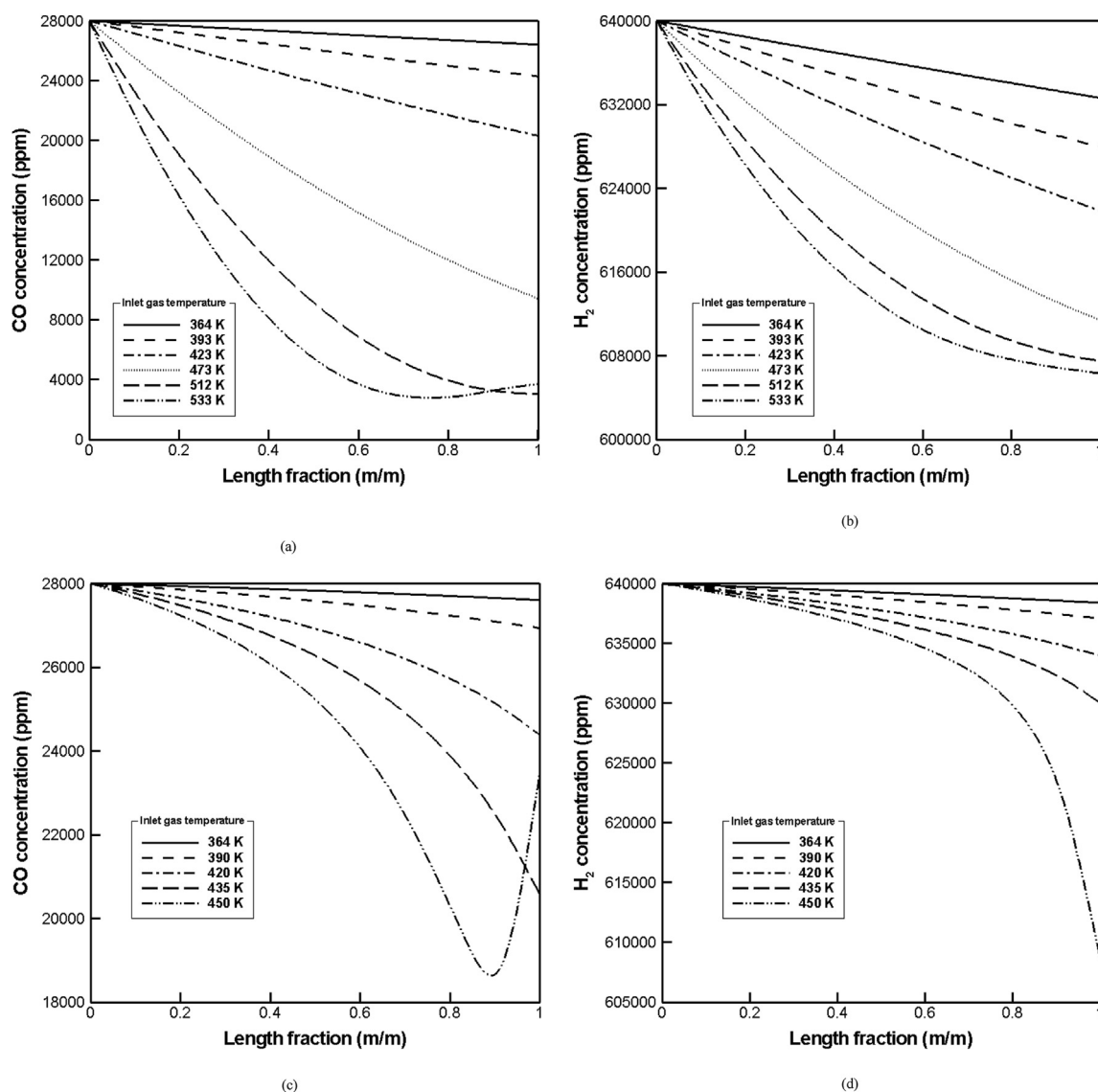


**Fig. 6** – (a) CO and (b) H<sub>2</sub> concentrations in the isothermal reactor (GHSV = 75,000 h<sup>-1</sup>) and (c) CO and (d) H<sub>2</sub> concentrations of the adiabatic reactor (GHSV = 400,000 h<sup>-1</sup>) in the flow channel direction (CO/O<sub>2</sub> = 2.8/2.9).

512 K for the isothermal reactor ( $S_{CO} = 43\%$ ) and 442 K under adiabatic conditions ( $S_{CO} = 39\%$ ). Beyond this maximum, it diminishes gradually. Catalysts with high Fe content promote CO conversion and even higher O<sub>2</sub> conversion, although the CO selectivity decreases [11,27]. This finding makes sense because a high catalytic activity implies that high O<sub>2</sub> consumption is also achieved and, recalling Eq. (17), the CO selectivity decreases.

The adiabatic reactor's GHSV was set much higher than that of the isothermal reactor, as shown in Fig. 3, because the gas temperature steeply increases in the adiabatic reactor at low flowrates, which in turn promotes the RWGS significantly. Fig. 4 shows the influence of the GHSV on the RWGS for both isothermal and adiabatic reactors along the flow direction. The GHSV had a negligible impact on the isothermal reactor's RWGS reaction, which was maintained almost uniform throughout the reactor, as shown in Fig. 4(a). By contrast, the RWGS becomes severe in the adiabatic

reactor, especially under lower GHSV conditions, as shown in Fig. 4(b).

#### Effect of inlet gas temperature

As shown in Fig. 3, a higher inlet temperature results in a greater RWGS, leading to degraded catalyst performance. Figs. 5(a) and 6(b) show the RWGS distribution as a function of the inlet gas temperature in both the isothermal and adiabatic reactors. Overall, the isothermal reactor showed uniformly elevated distributions of RWGS according to the inlet gas temperature, whereas the adiabatic reactor showed steeply increasing distributions of RWGS as the gas temperature increases along the flow direction.

Fig. 5(c) shows the wall temperature distribution of the adiabatic reactor according to the inlet gas temperature when CO/O<sub>2</sub> ratio and GHSV are 2.8/2.9 and 400,000 h<sup>-1</sup>, respectively. Because the exothermic reaction is promoted with an increase in the inlet gas temperature, the wall

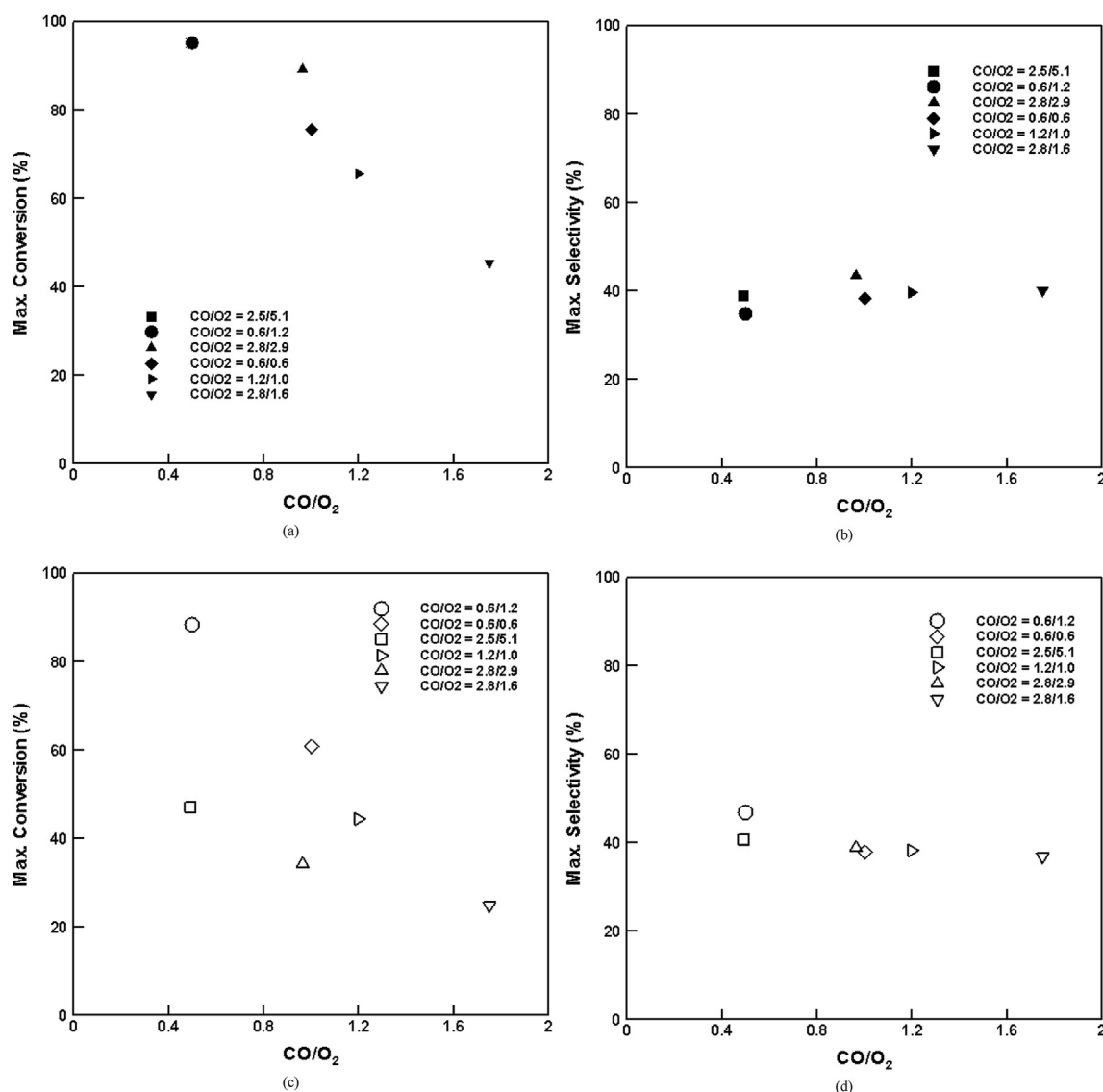


Fig. 7 – Maximum CO (a) conversion and (b) selectivity in the isothermal reactor (GHSV = 75,000 h<sup>-1</sup>). Maximum CO (c) conversion and (d) selectivity in adiabatic reactor (GHSV = 400,000 h<sup>-1</sup>).

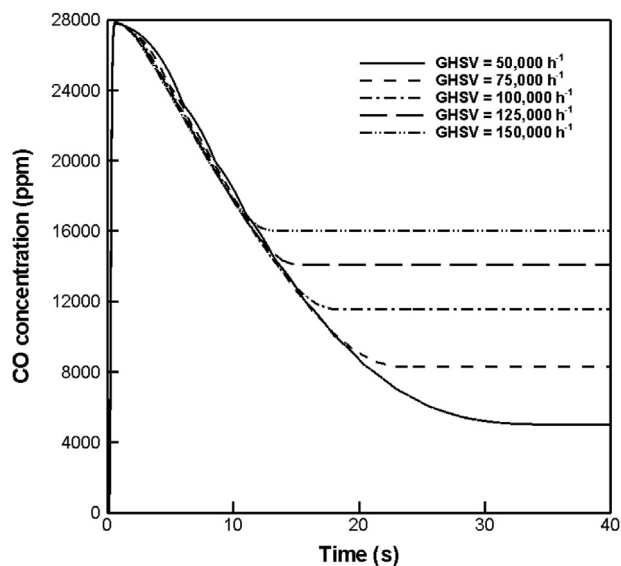
temperature rises sharply. The effect of the inlet gas temperature on the species concentration distribution is presented in Fig. 6. Both CO and H<sub>2</sub> concentrations gradually decrease, reaching the minimum concentration at the highest temperature, which shows the importance of the CO selectivity of the catalyst to minimize the loss of H<sub>2</sub>. When the inlet gas temperature is 450 K, the CO concentration shifts to increase at the outlet section of the reactor where the reactor temperature is very high, and RWGS is significant, as shown in Figs. 6(a) and 7(c).

#### Effect of CO/O<sub>2</sub> feed ratio

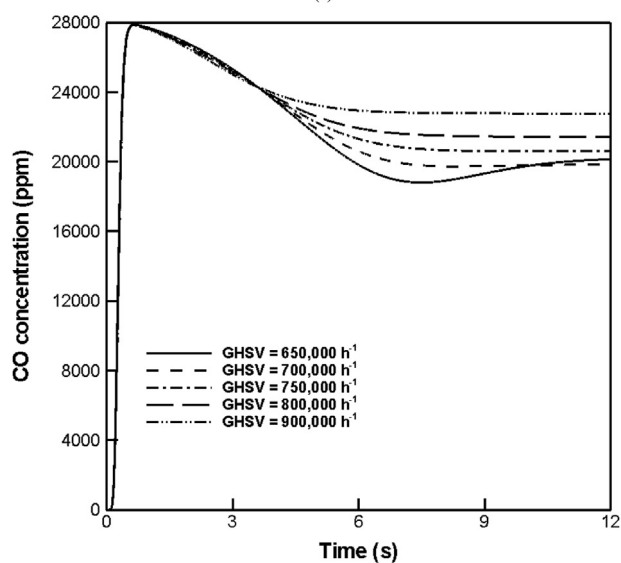
The maximum CO conversion and selectivity as a function of the CO/O<sub>2</sub> feed ratio for both isothermal and adiabatic reactors were obtained from the reactor performance analysis in Fig. 3. Overall, the maximum CO conversion was improved at low CO/O<sub>2</sub> ratios, especially with low inlet CO concentration, as

shown in Figs. 7(a) and 8(c). The adiabatic reactor achieved a high conversion efficiency when the CO/O<sub>2</sub> ratio and CO concentration were low (CO/O<sub>2</sub> = 0.6/1.2), as shown in Fig. 7(c). Meanwhile, the isothermal reactor achieved a high conversion efficiency even under high CO concentration conditions, as shown in Fig. 7(a). According to Eq. (4), the CO oxidation improves at low CO and high O<sub>2</sub> concentrations, promoting heat generation<sup>4</sup>. Under moderately controlled temperature conditions, the CO production through the RWGS reaction has less influence on the CO conversion rate. It was predicted that the isothermal reactor with low GHSV could achieve a high CO-PROX performance owing to the longer residence time of gas species on the catalyst washcoat when CO and O<sub>2</sub> concentrations increase.

Compared to the CO conversion, CO selectivity is not strongly affected by the CO/O<sub>2</sub> ratio regardless of the inlet CO concentration, as shown in Figs. 7(b) and 8(d), because



(a)



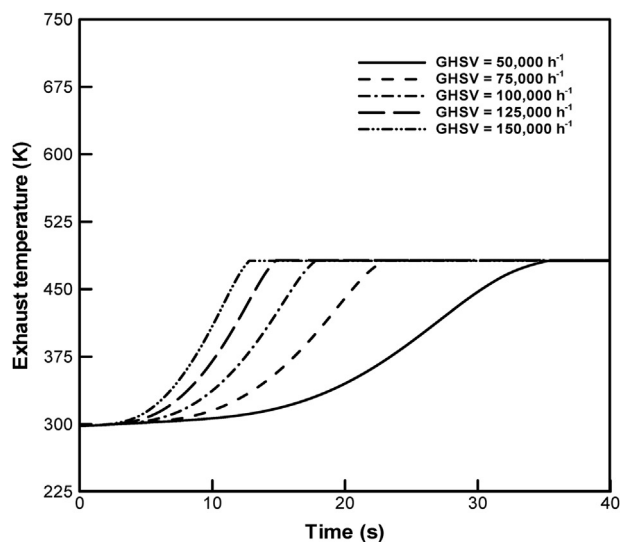
(b)

**Fig. 8 – Dynamic response of CO concentration in (a) isothermal and (b) adiabatic reactors at different GHSV (CO/O<sub>2</sub> = 2.8/2.9; T<sub>in, g</sub> = 480 K).**

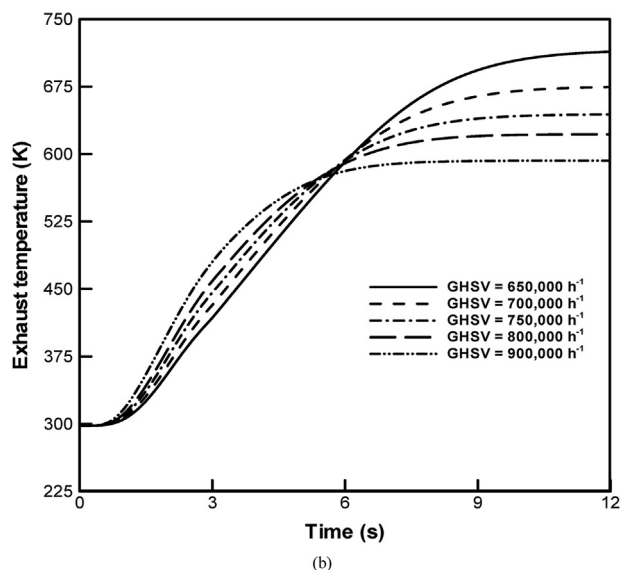
increasing the inlet concentration of O<sub>2</sub> promotes CO oxidation as well as H<sub>2</sub> oxidation, according to Eq. (17). The present CO conversion and selectivity agree well with the previously reported experimental results [2,8,33].

#### Dynamic response

The transient behavior of the CO-PROX reactor model was investigated under the following initial conditions ( $t_0 = 0$  s): i) zero flowrate, ii) reactor temperature ( $T_s$ ) of 298 K, and iii) activated Pt-Fe/ $\gamma$ -Al<sub>2</sub>O<sub>3</sub> catalyst. The reactors were operated with CO/O<sub>2</sub> = 2.8/2.9 and T<sub>inlet</sub> = 480 K. In addition, the required chemical properties are summarized in Table 2.



(a)



(b)

**Fig. 9 – Dynamic response of exhaust temperature of the (a) isothermal and (b) adiabatic reactors at different GHSV (CO/O<sub>2</sub> = 2.8/2.9; T<sub>in, g</sub> = 480 K).**

CO-PROX reactors are mainly used in on-board hydrogen production systems connected to a fuel cell scheme, implying that the GHSV varies with fuel demand. Figs. 8 and 9 demonstrate the dynamic response of both isothermal and adiabatic reactors with respect to the GHSV. Simulations were conducted until the dynamic response of the reactors approached the saturated value. Because the adiabatic reactor undergoes a severe RWGS that leads to low CO conversion under low flowrate conditions, much higher GHSV was supplied to the adiabatic reactor than the isothermal reactor. The saturated results for CO concentration and exhaust temperature with the response time at different GHSVs are summarized in Table 4. The response time ( $\tau_c$ ) was acquired by measuring the time approaching 99% of the saturated CO concentration after disturbance. To account for the time

**Table 4 – Saturated values and transient response for CO-PROX with different GHSV disturbances.**

Isothermal reactor (CO/O <sub>2</sub> = 2.8/2.9)					
GHSV	50,000 h <sup>-1</sup>	75,000 h <sup>-1</sup>	100,000 h <sup>-1</sup>	125,000 h <sup>-1</sup>	150,000 h <sup>-1</sup>
CO concentration	5000 ppm	8306 ppm	11,568 ppm	14,095 ppm	16,042 ppm
Gas temperature	481 K				
Response time	35 s	23 s	18 s	15 s	13 s
Residence time	72E-03 s	48E-03 s	36E-03 s	29E-03 s	24E-03 s
Heat generation time	34.71 s	22.81 s	17.86 s	14.88 s	12.90 s
Adiabatic reactor (CO/O <sub>2</sub> = 2.8/2.9)					
GHSV	650,000 h <sup>-1</sup>	700,000 h <sup>-1</sup>	750,000 h <sup>-1</sup>	800,000 h <sup>-1</sup>	900,000 h <sup>-1</sup>
CO concentration	20,145 ppm	19,841 ppm	20,610 ppm	21,492 ppm	22,826 ppm
Gas temperature	714 K	670 K	639 K	616 K	589 K
Response time	12 s	10 s	9 s	8 s	7 s
Residence time	5.54E-03 s	5.14E-03 s	4.8E-03 s	4.5E-03 s	4.0E-03 s
Heat generation time	11.98 s	9.98 s	8.98 s	7.98 s	6.98 s

required for the gas phase in the catalyst, the residence time ( $\tau$ ) was determined with the inverse of GHSV as follows:

$$\tau = \frac{L}{\bar{u}} \quad (18)$$

The residence time shows that the catalytic reaction depends on the time the involved species spend on the catalytic surface. The physical timescales associated with the CO-PROX were derived considering the heat and mass balance equation (1)–(4), as shown in Eqs. (19)–(22).

$$\frac{dC_{i,g}}{dt} = \left(\frac{1}{\tau}\right) N_{\text{node}} (C_{i,g,\text{in}} - C_{i,g}) - \left(\frac{1}{\tau_m}\right) (C_{i,g} - C_{i,s}) \quad (19)$$

$$(1 - \varepsilon) \frac{dC_{i,s}}{dt} = \left(\frac{1}{\tau_m}\right) (C_{i,g} - C_{i,s}) + \frac{\rho_{\text{ref}}}{\rho_g} \left(\frac{1}{\tau_r}\right) \quad (20)$$

$$\tau_m = \left(\frac{D_H}{4h_m}\right)$$

$$\tau_r = \left(\frac{\rho_{\text{ref}}}{M_g \rho_s}\right) \sum_k (a_{i,k} r_k)^{-1}$$

$$\frac{dT_g}{dt} = \left(\frac{1}{\tau}\right) (T_{g,\text{in}} - T_g) - \frac{\rho_{\text{ref}} c_{p,\text{ref}}}{\rho_g c_{p,g}} \left(\frac{1}{\tau_k}\right) (T_g - T_s) \quad (21)$$

$$(1 - \varepsilon) \frac{dT_s}{dt} = \frac{\rho_{\text{ref}} c_{p,\text{ref}}}{\rho_s c_{p,s}} \left(\frac{1}{\tau_k}\right) (T_g - T_s) + \frac{c_{p,\text{ref}} T_{\text{ref}}}{c_{p,s}} \left(\frac{1}{\tau_q}\right) \quad (22)$$

$$\tau_k = \rho_{\text{ref}} c_{p,\text{ref}} \left(\frac{D_H}{4h}\right)$$

$$\tau_q = c_{p,\text{ref}} T_{\text{ref}} \sum_k \left(r_k \Delta \bar{H}_k^0\right)^{-1}$$

Here,  $\tau_m$ ,  $\tau_r$ ,  $\tau_k$ , and  $\tau_q$  denote the mass convection, reaction, heat convection, and heat generation times, respectively. The gas density ( $\rho_{\text{ref}}$ ) and specific heat ( $c_{p,\text{ref}}$ ) were evaluated at the reference temperature ( $T_{\text{ref}}$ ) for a given composition, that is, the initial conditions. T'ien et al. [34] reported that the reaction timescale has the same order of magnitude as the residence time and equals the mass

convection time. In addition, Hayes et al. [35] pointed out that the timescale for the accumulation of heat by a solid is significantly longer than that of a gas, allowing us to disregard transient effects in the gas phase in Eq. (21). Because the order of magnitude of residence time is on the millisecond scales, the response time relies mainly on the heat generation timescale.

Notably, increasing the GHSV led to shorter response and residence times at higher CO concentrations at the reactor outlet. The response time of the isothermal reactor was much longer than that of the adiabatic reactor because of the low GHSV, as shown in Fig. 8. After an initial decrease in CO concentration, the adiabatic reactor experienced an increase in CO concentration at lower flowrate conditions (650,000 h<sup>-1</sup>) after  $t = 7.5$  s because of the rapidly increasing reactor temperature, resulting in a high RWGS, as shown in Figs. 8(b) and 9(b).

When a hydrogen production system such as a steam reforming reactor undergoes a load fluctuation, the byproduct CO gas concentration changes accordingly. To investigate the dynamic influence of the inlet CO concentration on the CO-PROX reactor, the isothermal and adiabatic reactors were subjected to changes in the CO/O<sub>2</sub> ratio, as shown in Figs. 10 and 11. As summarized in Table 5, the isothermal CO-PROX was predicted to require a shorter response time as the inlet O<sub>2</sub> concentration increases. The isothermal reactor was conditioned to reach the steady-state once the reactor wall temperature was equal to the gas temperature (425 K), i.e., the heat generation timescales were limited to values in Table 5. By contrast, the adiabatic reactor showed a longer response time when the inlet O<sub>2</sub> concentration increased as the reactor wall temperature reached a steady-state once the heat generation stabilized. According to Eqs. (10) and (11), the CO and H<sub>2</sub> oxidation rates increase with an increase in O<sub>2</sub> concentration, leading to higher heat generation, so the wall temperature took longer to reach a steady state.

The adiabatic CO-PROX experienced an increase in CO concentration and exhaust temperature after  $t = 10$  s at CO/O<sub>2</sub> = 2.5/5.1 because of the abrupt increase in the RWGS reaction at high temperatures, as shown in Fig. 10(b).

To investigate the effect of the inlet temperature on the dynamics further, the adiabatic CO-PROX reactor was

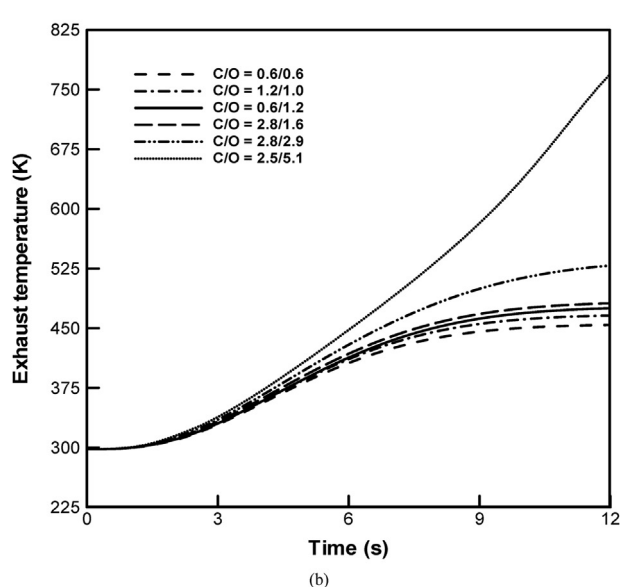
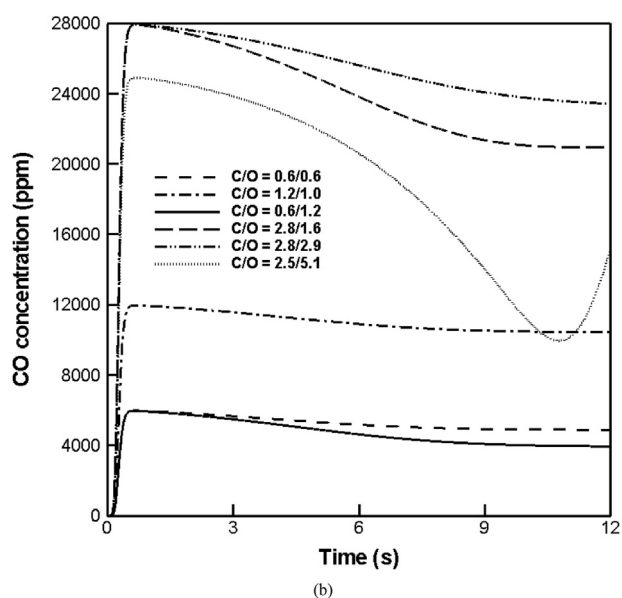
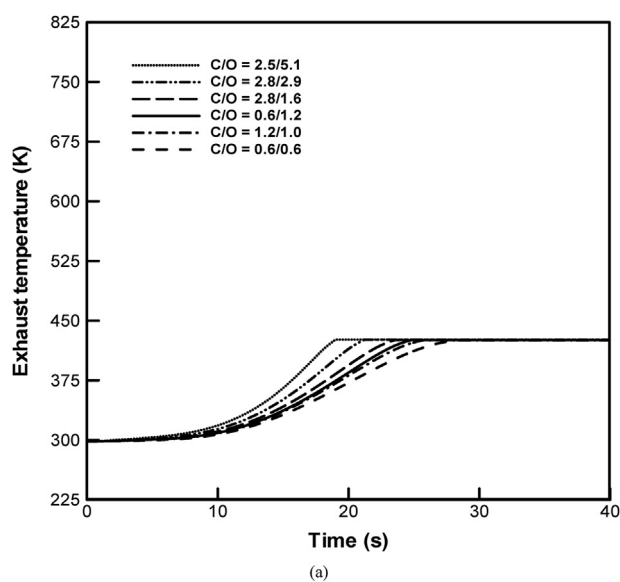
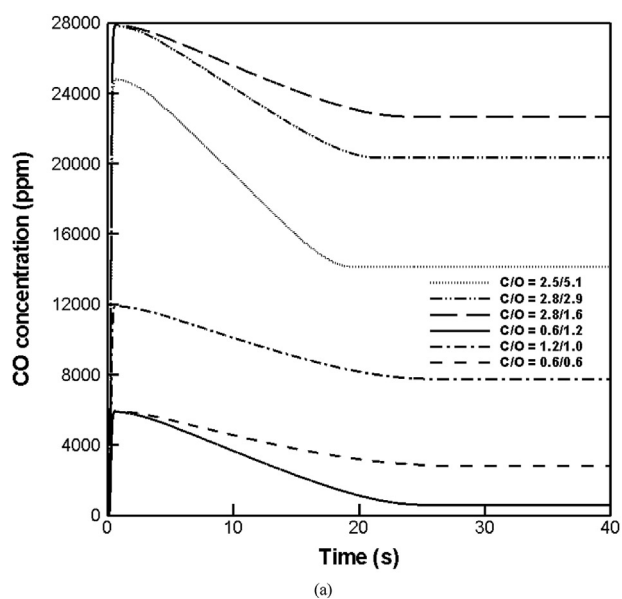


**Fig. 10** – Dynamic responses of CO concentration for the (a) isothermal ( $\text{GHSV} = 75,000 \text{ h}^{-1}$ ) and (b) adiabatic ( $\text{GHSV} = 400,000 \text{ h}^{-1}$ ) reactors at different inlet  $\text{CO}/\text{O}_2$  ratios ( $T_{\text{in, g}} = 425 \text{ K}$ ).

**Fig. 11** – Dynamic responses of exhaust temperature of the (a) isothermal ( $\text{GHSV} = 75,000 \text{ h}^{-1}$ ) and (b) adiabatic ( $\text{GHSV} = 400,000 \text{ h}^{-1}$ ) reactors at different inlet  $\text{CO}/\text{O}_2$  ratios ( $T_{\text{in, g}} = 425 \text{ K}$ ).

subjected to a step temperature profile from 435 to 455 to 400 K as shown in Fig. 12(a), corresponding to the same reactor response time ( $\tau_c = 15 \text{ s}$ ). As the inlet temperature increased from 435 to 455 K ( $\Delta T = 20 \text{ K}$ ), the CO concentration suddenly dropped by 78.9%, but the gas temperature rose by 12.6% at the reactor outlet. When the inlet gas temperature returned to 435 K, the CO concentration and temperature in the exhaust gas also returned to the initial value. By contrast, when the inlet gas temperature was decreased from 435 to 400 K ( $\Delta T = 35 \text{ K}$ ), the CO concentration increased by 57.7%, and the exhaust temperature decreased by 14.1%. From this observation, it was predicted that a larger change in CO concentration could be achieved with smaller inlet gas temperature change (435–455 K) than with larger inlet gas temperature change

(435–400 K). This high CO-PROX sensitivity in the first temperature range (435–455 K) suggests that an increase in CO conversion from 435 K is possible with a small amount of additional energy (minimum change in the inlet gas temperature) without adversely affecting the reactor response time, which is useful for power optimization and control.

To test the present CO-PROX model under realistic operating conditions, a simulation was performed based on the transient fuel demand in a PEM fuel cell system. Soumeur et al. [36] studied the PEM fuel cell performance using a dynamic speed cycle for electric vehicles and obtained a hydrogen-rich fuel consumption scheme, as shown in

**Table 5 – Steady-state values and transient response for CO-PROX at different CO/O<sub>2</sub> ratios.**

Isothermal reactor (GHSV = 75,000 h <sup>-1</sup> )						
CO/O <sub>2</sub>	2.5/5.1	2.8/2.9	2.8/1.6	0.6/1.2	12.2/1.0	0.6/0.6
CO concentration	14,151 ppm	20,334 ppm	22,685 ppm	595 ppm	7751 ppm	2809 ppm
Gas temperature	425 K					
Response time	19.31 s	21.44 s	23.8 s	25 s	26 s	28.35 s
Residence time	48E-03 s					
Heat generation time	19.12 s	21.25 s	23.61 s	24.81 s	25.81 s	28.158 s
Adiabatic reactor (GHSV = 400,000 h <sup>-1</sup> )						
CO/O <sub>2</sub>	0.6/0.6	1.2/1.0	0.6/1.2	2.8/1.6	2.8/2.9	2.5/5.1
CO concentration	4900 ppm	10,470 ppm	3976 ppm	20,950 ppm	23,429 ppm	15,220 ppm
Gas temperature	446 K	461 K	471 K	480 K	528 K	770 K
Response time	9 s	10 s	10.5 s	11.35 s	12 s	12 s
Residence time	9E-03 s					
Heat generation time	8.96 s	9.96 s	10.46 s	11.31 s	11.96 s	11.96 s

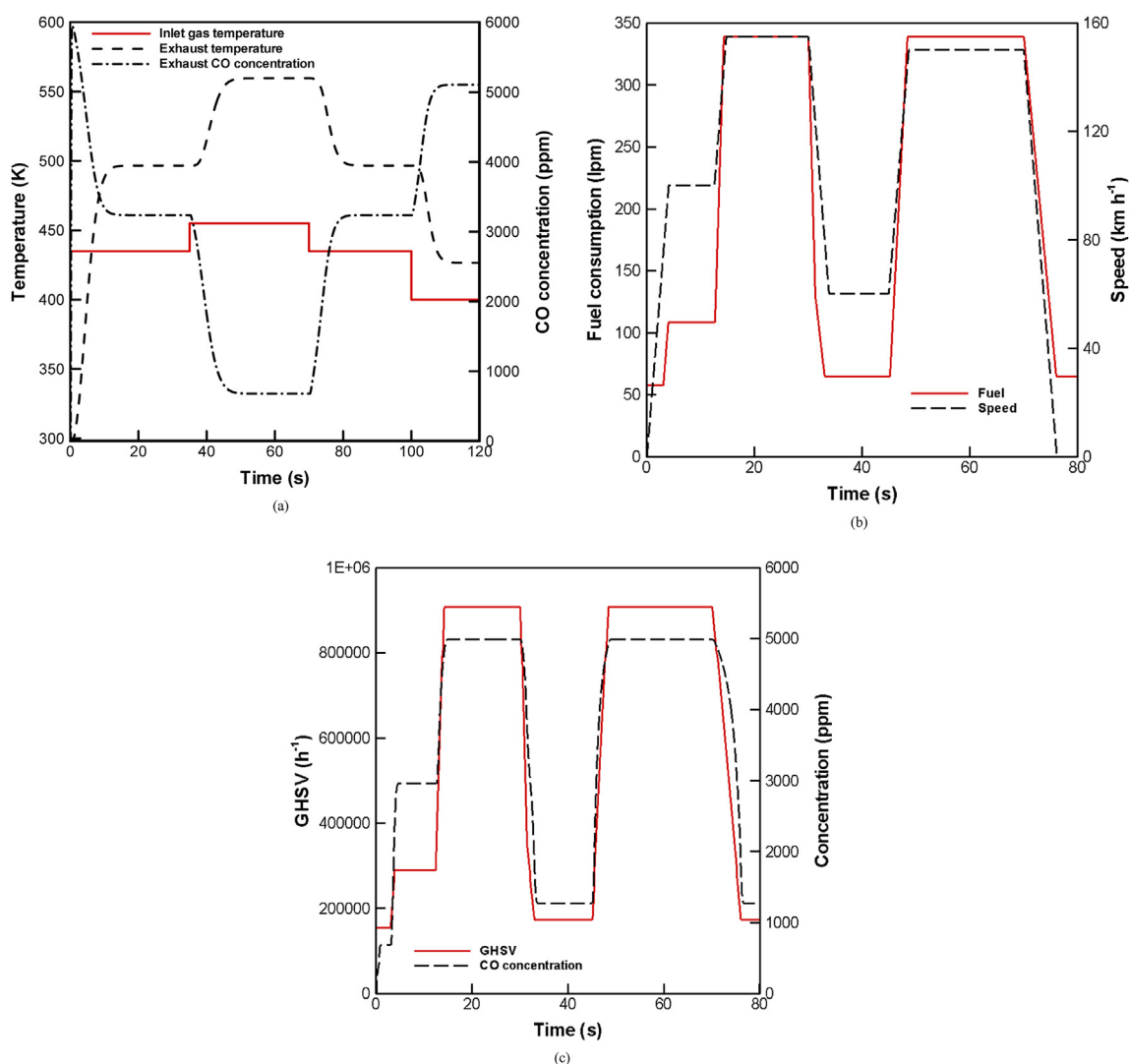


**Fig. 12 – Dynamic responses for (a) adiabatic CO-PROX to step changes in inlet gas temperature (GHSV = 400,000 h<sup>-1</sup>; CO/O<sub>2</sub> = 0.6/1.2), (b) Fuel consumption scheme for electric vehicles [36], and (c) isothermal CO-PROX to step changes according to the gas hourly space velocity ( $T_{in, g} = 520$  K; CO/O<sub>2</sub> = 0.6/1.2).**

Fig. 12(b). For automotive applications, commercial monolithic reactors with a cordierite substrate generally contain 900 cells per square inch (cps) [37]. Kingsbury et al. [38] tested monolithic ceramic substrates and found that 900 cps reactors reach a GHSV of 60,000 h<sup>-1</sup> at a flow rate of 22.4 l min<sup>-1</sup>. Thus, the fuel consumption profile was transformed into a GHSV scheme for simulation purposes, as shown in Fig. 12(c). The dynamic simulation was performed in the isothermal CO-PROX model, assuming that the time-dependence of gas and surface temperatures in Eqs. (3) and (4) is null, and Damköhler number (ratio of reaction rate to convection mass transport rate) approaches unity [39]. Thus, Eq. (2) can be simplified as Eq. (23).

$$\frac{4h_{m,i}}{D_H} (C_{i,g} - C_{i,s}) = -M_g \frac{\rho_s}{\rho_g} \sum_k (a_{i,k} r_k) \quad (23)$$

Subsequently, Eq. (1) is modified, and Eq. (24) is obtained.

$$\frac{dC_{i,g}}{dt} = \left(\frac{1}{\tau}\right) N_{\text{node}} (C_{i,g,\text{in}} - C_{i,g}) + \frac{\rho_{\text{ref}}}{\rho_g} \left(\frac{1}{\tau_r}\right) \quad (24)$$

Therefore, the rate of changes of the outlet gas concentration mainly depends on the residence and reaction time-scales, as long as the wall temperature and bulk gas temperature are previously in equilibrium ( $T_s = T_g$ ). Equation (24) explains the fast response at each GHSV shift in Fig. 12(b) because the residence and reaction time are on the order of milliseconds.

As predicted, a high space velocity resulted in lower CO conversion performance. To protect the hydrogen fuel cell catalysts from CO contamination, the use of a multi-stage CO-PROX H<sub>2</sub> supply system is desirable. Further, the inlet gas temperature must be adjusted at higher GHSVs to obtain higher CO conversion. Finally, a thermal management system is necessary to control the reactor temperature to suppress the RWGS reaction.

## Conclusions

A quasi-2D, dynamic model of the CO-PROX for H<sub>2</sub> production was developed and simulated to elucidate the effect of operating conditions such as flow rate, inlet temperature, and gas concentration on the CO-PROX performance. The developed model was validated with experimental data, which confirmed the high fidelity of the model. The following conclusion were drawn from the parametric study using the developed model.

- At different inlet gas temperatures, the CO-PROX reactor was simulated under both isothermal and adiabatic conditions. Maximum CO conversion and selectivity were obtained first, followed by a gradual decrease at higher inlet gas temperatures.
- Although the GHSV had a negligible impact on the RWGS in the isothermal reactor, the RWGS became severe below a GHSV of 400,000 h<sup>-1</sup> in the adiabatic reactor.
- When operated at different inlet gas temperatures, the adiabatic reactor showed an increasing RWGS distribution and wall temperature along the flow direction.

- Overall, the maximum CO conversion was improved with low CO/O<sub>2</sub> ratios. However, CO selectivity was barely affected by the CO/O<sub>2</sub> ratio.
- High GHSVs caused short timescales with high CO concentrations in both isothermal and adiabatic reactors, but the adiabatic reactor had even shorter response times.
- Although the isothermal CO-PROX required a shorter response time as the inlet O<sub>2</sub> concentration increased, this resulted in longer response times for the adiabatic reactor.
- The high response sensitivity of the adiabatic CO-PROX reactor allowed higher CO conversion from 435 K with small additional energy, holding the response time at 15 s.
- The isothermal reactor exhibited a reasonably fast response time when exposed to a realistic GHSV scheme based on the transient fuel demand in a PEM fuel cell system. Multi-stage CO-PROX and gas temperature control are suggested for an H<sub>2</sub> system.

## Declaration of competing interest

The authors declare that they have no known competing financial interests or personal relationships that could have appeared to influence the work reported in this paper.

## Acknowledgement

This work was financially supported by the National Research Foundation of Korea (No. 2019R1A2C1090828 and 2020R1A5A8018367) and the Korea Institute for Advancement of Technology (No. S2640194).

## Nomenclature

### List of symbols

$a$	stoichiometric coefficient of species in reactions
$A$	pre-exponential factor
$A_c$	cross-sectional area, m <sup>2</sup>
$c_p$	specific heat, J kg <sup>-1</sup> K <sup>-1</sup>
$C$	concentration, (moles of species) (total moles in a gas mixture) <sup>-1</sup>
$D$	diffusion coefficient, m <sup>2</sup> s <sup>-1</sup>
$D_H$	hydraulic diameter, m
$E_a$	activation energy, J mol <sup>-1</sup>
$f_D$	second-order corrector
$h$	heat transfer coefficient, W m <sup>-2</sup> K <sup>-1</sup>
$h_m$	mass transfer coefficient, m s <sup>-1</sup>
$\Delta H$	enthalpy of reaction, J mol <sup>-1</sup>
$k_g$	gas thermal conductivity, W m <sup>-1</sup> K <sup>-1</sup>
$k$	rate constant, mol kg <sup>-1</sup> s <sup>-1</sup>
$K_{\text{eq}}$	equilibrium constant
$L$	total reactor length, m
$M$	molecular weight, kg mol <sup>-1</sup>
$N_{\text{node}}$	number of nodes of the model
$p$	perimeter, m
$P$	pressure, Pa
$r$	reaction rate, mol kg <sup>-1</sup> s <sup>-1</sup>

$R_u$	universal constant of gases, $8.314 \text{ J mol}^{-1} \text{ K}^{-1}$
$t$	time, s
$T$	temperature, K
$S$	selectivity, %
$\bar{u}$	uniform average velocity, $\text{m s}^{-1}$
$x$	length coordinate, m
$\Delta x$	volume element length, m
$X$	conversion rate, %
$y$	molar fraction

#### Greek letters

$\alpha, \beta, \gamma$	apparent reaction orders
$\varepsilon$	porosity
$\varepsilon_{oAB}$	Lennard–Jones energy constant, J
$\kappa$	Boltzmann gas constant, $\text{J K}^{-1}$
$\mu$	viscosity, Pa s
$\lambda$	stoichiometric ratio
$\rho$	density, $\text{kg m}^{-3}$
$\sigma$	Lennard–Jones length constant, m
$\varphi$	function of molecular weights and viscosities of the mixture components
$\tau$	residence time, s
$\tau_c$	response time, s
$\tau_r$	reaction time, s
$\tau_m$	mass convection time, s
$\tau_k$	heat convection time, s
$\tau_q$	heat generation time, s

#### Superscripts and subscripts

g	gas phase
i	number (integer)
in	inlet
j	number (integer)
k	number (integer)
out	outlet
s	solid phase
0	standard condition

#### Abbreviations

2D	two dimensional
GHSV	gas hourly space velocity
NIST	National Institute of Standards and Technology
ODE	ordinary differential equation
PROX	preferential oxidation
PDE	partial differential equation
RWGS	reverse water gas shift

## Appendix A. Transport properties

Because the heat- and mass-transfer coefficients are calculated from the Reynolds ( $Re$ ), Nusselt ( $Nu_{H_{1,\infty}}$ ), and Sherwood ( $Sh_{H_{1,\infty}}$ ) numbers, and hydraulic diameter  $D_H = 4A_c/p$ ,  $Nu_{H_{1,\infty}}$  and  $Sh_{H_{1,\infty}}$  are fixed equal to 3.608 for fully developed laminar flow ( $Re < 2300$ ) and square cross-section all along the single-stage CO-PROX reactor. The heat- and mass-transfer coefficients are defined as

$$\bar{h} = \frac{Nu_{1,\infty} k_g}{D_H} \quad (25)$$

$$h_m = \frac{Sh_{H_{1,\infty}} D_{AB}}{D_H} \quad (26)$$

Different theoretical models are available for computing the diffusion coefficient of a binary-gas mixture  $D_{AB}$ . For non-polar molecules, the Lennard–Jones potential offers a basis for obtaining the diffusion coefficients of binary gas mixtures. The mutual diffusion coefficient of species A and B is defined as [25].

$$D_{AB} = 0.001858 T^{3/2} \sqrt{\frac{M_A + M_B}{M_A M_B}} \frac{f_D}{P \sigma_{AB}^2 \Omega_D} \quad (27)$$

where  $f_D$  is the second-order corrector and  $\Omega_D$  is the collision integral, which is defined as [26].

$$\Omega_D = \frac{1.06036}{(T^*)^{0.15610}} + \frac{0.19300}{\exp(0.47635T^*)} + \frac{1.03587}{\exp(1.52996T^*)} + \frac{1.76474}{\exp(3.89411T^*)}$$

where  $T^* = \frac{\kappa T_g}{\varepsilon_{oAB}}$  and  $\varepsilon_{oAB} = (\varepsilon_{oA} \varepsilon_{oB})^{1/2}$ .

(28)

The calculation for the binary diffusion coefficient under different pressure and temperature conditions is as follows:

$$D_{AB} = D_{AB,0} \left( \frac{T_g}{T_0} \right)^{3/2} \left( \frac{P}{P_0} \right)^{-1} \quad (29)$$

Owing to the presence of multiple species in the gas mixture, the diffusion coefficient for the species  $i$  in the mixture is related to the binary diffusion coefficients, as expressed by Blanc's Law [26]:

$$D_i = \left( \sum_{\substack{j=1 \\ j \neq i}}^n \frac{y_j}{D_{ij}} \right)^{-1} \quad (30)$$

By considering small temperature and pressure gradients along with the volume element, the density of the mixture is calculated based on an ideal-mixture state equation at the working temperature and pressure, as follows:

$$\rho_g = \frac{P M_g}{R_u T_g} \quad (31)$$

Hence,  $M_g$  is determined by

$$M_g = \sum_i^n y_i M_i \quad (32)$$

In addition, the gas phase thermophysical properties, including the constant-pressure specific heat, thermal conductivity, dynamic viscosity, and Prandtl number, are evaluated based on the properties of the individual species using Eqs. (33)–(37).

$$C_{p,g} = \sum_i^n y_i C_{p,i} \quad (33)$$

$$k_g = \sum_i^n \left( \frac{k_{g,i}}{1 + \frac{1}{y_i} \sum_j \varphi_{i,j} y_j} \right) \quad (34)$$

$$\mu_g = \sum_i^n \left( \frac{\mu_i}{1 + \frac{1}{y_i} \sum_j \varphi_{i,j} y_j} \right) \quad (35)$$

$$\varphi_{i,j} = \frac{\left\{ 1 + \left( \frac{\mu_i}{\mu_j} \right)^{1/2} \left( \frac{M_i}{M_j} \right)^{1/4} \right\}^2}{\left\{ 8 \left( 1 + \frac{M_i}{M_j} \right) \right\}^{1/2}} \quad (36)$$

$$Pr = \frac{\mu_g C_{p,g}}{k_g} \quad (37)$$

## REFERENCES

- [1] Yan Y, Thanganadar D, Clough PT, Mukherjee S, Patchigolla K, Manovic V, Anthony EJ. *Energy Convers Manag* 2020;222:113144.
- [2] Caputo T, Lisi L, Pirone R, Russo G. *Ind Eng Chem Res* 2007;46(21):6793.
- [3] Cipiti F, Recupero V. *Chem Eng J* 2009;146:128.
- [4] Liu K, Wang A, Zhang T. *ACS Catal* 2012;2(6):1165.
- [5] Galletti C, Specchia S, Specchia V. *Chem Eng J* 2011;167:616.
- [6] Saavedra J, Whittaker T, Chen Z, Purcell C, et al. *Nat Chem* 2016;8(6):584.
- [7] Luengnaruemitchai A, Srihamat K, Pojanavaraphan C, Wanchanthuek R. *Int J Hydrogen Energy* 2015;40(39):13443.
- [8] Choi Y, Stenger HG. *J Power Sources* 2004;129:246.
- [9] Avgouropoulos G, Ioannides T, Papadopoulou Ch, Batista J, Hocevar S, Matralis HK. *Catal Today* 2002;75:157.
- [10] Rossetti I, Bahadori E, Tripodi A, Ramis G. *Materials* 2019;12:884.
- [11] Roberts GW, Chin P, Sun X, Spivey JJ. *Appl Catal, B* 2003;46:601.
- [12] Chen J, Yang H, Wang N, Ring Z, Dabros T. *Appl Catal, A* 2008;345:1.
- [13] Ahluwalia RK, Zhang Q, Chmielewski DJ, Lauzze KC, Inbody MA. *Catal Today* 2005;99:271.
- [14] Jeifetz LG, Giunta PD, Mariño FJ, Amadeo NE, Laborde MÁ. *Int J Chem React Eng* 2014;12(1):1.
- [15] Moreno M, Baronetti G, Laborde M, Mariño F. *Int J Hydrogen Energy* 2008;33:3538.
- [16] Almeida Pazmiño GA, Jung S. *Energy Convers Manag* 2019;192:269.
- [17] Xu G, Zhang ZG. *J Power Sources* 2006;157(1):64.
- [18] Salomons S, Hayes RE, Votsmeier M. *Appl Catal, A* 2009;352:27.
- [19] Bhatia D, Harold MP, Balakotaiah V. *Chem Eng Sci* 2009;64(7):1544.
- [20] Moe JM. *Chem Eng Prog* 1962;58:33.
- [21] Ghosh S, Singh MP, Mohanty UC. *Boundary-Layer Meteorol* 1986;34:311.
- [22] Poling BE, Prausnitz JM, O'Connell JP. *The properties of gases and liquids*. 5<sup>th</sup> ed. Mc Graw Hill; 2011.
- [23] Korotkikh O, Farrauto R. *Catal Today* 2000;62(2–3):249.
- [24] Hultberg PC, Brandin JGM, Silversand FA, Lundberg M. *Int J Hydrogen Energy* 2005;30(11):1235.
- [25] Nibbelke RH, Campman MAJ, Hoebink JHBJ, Marin GB. *J Catal* 1997;171:358.
- [26] Manasilp A, Gulari E. *Appl Catal B: Environ* 2002;37(1):17.
- [27] Capannelli G, Carosini E, Cavani F, Montecelli O, Trifiro F. *Chem Eng Sci* 1996;51(10):1817.
- [28] Guo W, Xiao W, Luo M. *Chem Eng J* 2012;207:734.
- [29] Lee HC, Kim DH. *Catal Today* 2008;132(1–4):109.
- [30] T'ien JS. *Combust Sci Technol* 1981;26(1–2):65.
- [31] Bennett CJ, Hayes RE, Kolaczowski ST. *Proc Roy Soc Lond A* 1992;439:465.
- [32] Soumeur MA, Gasbaoui B, Abdelkhalek O, Ghouili J, Toumi T, Chakar A. *J Power Sources* 2020;462:228167.
- [33] Boger T, Heibel AK, Sorensen CM. *Ind Eng Chem Res* 2004;43(16):4602.
- [34] Kingsbury B, Stewart J, Wu Z, Douglas R, Li K. *SAE Tech Paper* 2014-01-2805 2014.
- [35] Joshi SY, Harold MP, Balakotaiah V. *AIChE J* 2009;55(7):1771.